New structural features of the APC/C revealed by high resolution cryo-EM structures of apo-APC/C and the APC/C$^{CDH1:EMI1}$ complex

Anna Höfler[1,5], Jun Yu[1,5], Jing Yang[2], Ziguo Zhang[2], Leifu Chang[2], Geoffrey W. Grime[3], Elspeth F. Garman[4], Andreas Boland[1,6] and David Barford[2,6]

[1]Department of Molecular and Cellular Biology, University of Geneva, Geneva, Switzerland.

[2]MRC Laboratory of Molecular Biology, Cambridge, CB2 0QH, UK.

[3]Ion Beam Centre, Advanced Technology Institute, University of Surrey, Guildford, Surrey GU2 7XH, UK.

[4]Department of Biochemistry, Dorothy Crowfoot Hodgkin Building, South Parks Road, University of Oxford, Oxford, OX1 3QU, UK.

[5]These authors contributed equally.

[6]Corresponding authors. email: Andreas.Boland@unige.ch; dbarford@mrc-lmb.cam.ac.uk

Abstract

The multi-subunit anaphase-promoting complex/cyclosome (APC/C) is a master regulator of cell division. It controls progression through the cell cycle by timely marking mitotic cyclins and other cell cycle regulatory proteins for degradation via the ubiquitin-proteasome pathway. The APC/C itself is regulated by the sequential action of its coactivator subunits CDC20 and CDH1, post-translational modifications, and its inhibitory binding partners EMI1 and the mitotic checkpoint complex (MCC). In this study, we took advantage of the latest developments in cryo-electron microscopy (cryo-EM) to determine the structures of human APC/C$^{CDH1:EMI1}$ and apo-APC/C at 2.9 Å and 3.2 Å, respectively, providing novel insights into the regulation of APC/C activity. The high resolution maps allowed the unambigious assignment of a previously unassigned α-helix to the N-terminus of CDH1 (CDH1$^{\alpha1}$) in the APC/C$^{CDH1:EMI1}$ ternary complex. CDH1$^{\alpha1}$ binds at the APC1:APC8 interface, thereby interacting with a loop segment of APC1 through electrostatic interactions only provided by CDH1 but not CDC20. We also indentified a novel zinc-binding module in APC2, and confirmed the presence of zinc ions experimentally. Finally, due to the higher resolution and well defined density of these maps we were able to build, aided by AlphaFold predictions, several intrinsically disordered regions in different APC/C subunits that play a fundamental role in proper complex assembly.

Introduction

The anaphase-promoting complex/cyclosome (APC/C) is a large multi-subunit complex that functions as an E3 ubiquitin ligase to regulate transitions through the cell cycle, achieved by controlling the defined ubiquitin-dependent degradation of specific cell cycle regulators. APC/C activity and substrate selection are controlled at various levels to ensure that specific cell cycle events occur in the correct order and time. These regulatory mechanisms include the binding of cell cycle specific coactivator subunits (CDC20 and CDH1), reversible APC/C and coactivator phosphorylation, inhibitory complexes and proteins (for example the mitotic checkpoint complex (MCC) and early mitotic inhibitor 1 (EMI1)), and APC/C SUMOylation, reviewed in [1-4].

Defined protein degradation controlled by the APC/C regulates the metaphase to anaphase transition. In mitosis, the APC/C is activated by phosphorylation and by the binding of a coactivator subunit CDC20, to form the APC/C^{CDC20} complex. The key role of APC/C^{CDC20} is to ubiquitinate securin and

cyclin B. These proteins inhibit the protease separase. APC/C-mediated destruction of both securin and cyclin B activates separase to cleave the cohesin ring, thereby triggering sister chromatid segregation and the onset of anaphase [5]. During this transition, the APC/C and CDH1 are dephosphorylated, resulting in a switch from APC/C^{CDC20} to APC/C^{CDH1}. In addition to its roles regulating the metaphase to anaphase transition, the APC/C regulates the events of cytokinesis and the entry into G1.

The APC/C recognizes most of its substrates through destruction motifs or degrons: the D box, the ABBA motif and the KEN box. These motifs interact with their cognate receptors on the two structurally related WD40-domain coactivator subunits (CDC20 in mitosis and CDH1 in G1) that act as adaptors to recruit substrates to the APC/C. Control of different cell-cycle phases by the APC/C is mediated through the different substrate specificities of APC/C^{CDC20} and APC/C^{CDH1}. Additionally, substrate specificity of APC/C^{CDC20} is augmented by the MCC which inhibits APC/C^{CDC20} activity towards cyclin B and securin, but not cyclin A [6]. Two conserved motifs in both coactivators, a seven residue-N-terminal C box, and an extreme C-terminal Ile-Arg motif (IR tail), are necessary for coactivators to bind the APC/C. The APC/C is a cullin-RING E3 ubiquitin ligase, with the catalytic module composed of the cullin-domain APC2 subunit and the RING-domain APC11 subunit. In human, two different E2 enzymes (UBCH10/UBE2C and UBE2S) bind the catalytic module of the APC/C in close proximity to the substrate to catalyse subunit polyubiquitination. In vertebrates, EMI1 functions as an antagonist of APC/C^{CDH1} during S phase and G2 to allow cells to commit to DNA replication and cell division.

We had previously determined cryo-EM structures of human APC/C$^{CDH1:EMI1}$ (Ref. [7]) and unphosphorylated apo-APC/C [8], both at 3.6 Å resolution. Here, by taking advantage of the latest improvements in cryo-EM hardware and software, we determined the structures of APC/C$^{CDH1:EMI1}$ and apo-APC/C at 2.9 Å and 3.2 Å resolution, respectively. The well defined cryo-EM maps, as well as currently existing APC/C models combined with AlphaFold predictions [9,10], enabled us to build the most complete and accurate structural models of the APC/C available to date. Our new models reveal novel insights into APC/C regulation during mitosis, providing a more detailed structural rational for the phosphorylation-dependent switch from APC/C^{CDC20} to APC/C^{CDH1}, the identification of a novel zinc-binding module in APC2, and shed light on the role of intrinsically disordered regions (IDRs) in APC/C complex assembly.

Results and Discussion

Structure determination

Our previous cryo-EM reconstruction of the APC/C in complex with the coactivator CDH1 and the inhibitor EMI1 (APC/C$^{CDH1:EMI1}$) (PDB 4ui9) at 3.6 Å resolution [7], and a 3.6 Å resolution structure of the apo unphosphoryated APC/C [8] were determined using data collected on a Polara electron microscope equipped with a Falcon 2 detector. For the currrent study, we collected data on an APC/C$^{CDH1:EMI1}$ sample using a Titan Krios microscope with a Falcon 3 detector. These new data, together with the use of recently developed refinement methods (detailed in Methods), resulted in new reconstructions of the ternary APC/C$^{CDH1:EMI1}$ complex at 2.9 Å resolution, providing better definition of the numerous extended and loop structures that promote inter-subunit interactions, the discovery of a novel zinc-binding module in APC2, and definition of how the N-terminal α-helix of CDH1 binds to the APC1 subunit (**Fig. 1**).

For this study, the APC/C$^{CDH1:EMI1}$ ternary complex and cryo-EM grids were prepared as described previously [7] (**Supplementary Fig. 1**). The cryo-EM map refinement work-flow, based on a multi-body approach, is detailed in Methods (**Supplementary Fig. 2 and Supplementary Table 1**). Three dimensional classification generated eight 3D classes, two belonging to the APC/C$^{CDH1:EMI1}$ ternary

complex and two to the apo-APC/C state (that is without CDH1 and EMI1). The four remaining classes (classes 3-6; **Supplementary Fig. 2**) corresponded to incomplete APC/C assemblies. The APC/C$^{CDH1:EMI1}$ ternary complex map was divided into three masks, with some overlap, for particle subtraction and focussed 3D refinement. This process greatly improved cryo-EM densities in the more peripheral and flexible regions of the map. Specifically, well defined cryo-EM density is visible for the flexible catalytic module comprising the APC2 C-terminal domain (APC2^{CTD}), APC11 and the zinc-binding region (ZBR) of EMI1 (EMI1^{ZBR}) (**Fig. 1a, b and Supplementary Fig. 1c**). Additionally, the APC7 homo-dimer, capping the TPR lobe, is well defined. The new apo-APC/C structure at 3.2 Å supersedes the previously determined, phosphorylated and unphosphorylated apo-APC/C maps at 3.4 Å and 3.8 Å, respectively [8].

APC/C$^{CDH1:EMI1}$ ternary complex

As outlined in **Supplementary Table 2**, the new maps allowed marked improvements to regions of the structure compared to the previous 3.6 Å map [7] (PDB 4ui9) according to three main categories – (i) rebuilding of poorly defined loops; (ii) the fitting of side chains and hence residue assignment to previously built poly-Ala regions; (iii) *de novo* building of specific regions of the molecule. Four rebuilt or *de novo* built regions have biological implications and are discussed in more detail below.

1. **N-terminal α-helix of CDH1 (CDH1$^{\alpha1}$).** In the PDB code 4ui9 structure [7], we built a poly-Ala α-helix in density adjacent to the WD40 domain of APC1 (APC1^{WD40}), assigned to residues 282-295 of APC1. In the new map, the clearly defined side chain densities do not fit the APC1 sequence, but instead match the extreme N-terminal sequence of CDH1 (residues 1-19) (**Fig. 2a, b, d**). Secondary structure predictions, supported by an AlphaFold model [9,10], strongly confirm this region of human CDH1 to form an α-helix. This places the N-terminus of CDH1 on the outer surface of the APC/C. The CDH1 polypeptide chain then threads through a fenestration at the interface of APC6 and APC8 before forming the C-box motif that engages the C-box-binding site of APC8 (**Fig. 2a**). The remainder of CDH1, including the substrate-recognition degron-binding sites of CDH1^{WD40}, is positioned within the central cavity of the APC/C (**Fig. 1c**). Multiple sequence alignments (MSA) indicate CDH1$^{\alpha1}$ is highly conserved in metazoan CDH1 (**Fig. 2f**), supported by its prediction in AlphaFold models of metazoan CDH1 [10]. In contrast, the sequence corresponding to human CDH1$^{\alpha1}$ is neither conserved in budding yeast CDH1 (data not shown) nor is an N-terminal α-helix predicted in AlphaFold models of budding yeast CDH1 [10]. This is consistent with the 3.5 Å structure of the *S. cerevisiae* APC/C$^{CDH1:Hsl1}$ complex (PDB: 8A3T) (E. Vazquez-Fernandez, D. Barford *et al*., unpublished) that lacks cryo-EM density equivalent to CDH1$^{\alpha1}$ of human APC/C$^{CDH1:EM1}$. The amphipatic CDH1$^{\alpha1}$ helix interacts through non-polar interactions with a hydrophobic groove in the APC1^{WD40} domain via its N-terminal Met1, as well as Tyr5, Leu9 and Ile13 residues on one side of CDH1$^{\alpha1}$ (**Fig. 2b, c**). Residues Asp2, Asp4, Tyr5, Arg8, Arg11 and Gln12 on the opposite side of CDH1$^{\alpha1}$ form specific side chain-side chain interactions with the APC1^{WD40} domain as well as APC8B. Here, Arg8 plays a central role to anchor CDH1$^{\alpha1}$ by deeply inserting into an interface formed by both APC/C subunits APC1 and APC8B.

   AlphaFold models indicated that metazoan CDC20 also possesses a similar N-terminal α-helix to CDH1. Supporting this proposal, a reinterpretation of the 3.2 Å resolution cryo-EM maps of the phosphorylated APC/C$^{CDC20:CyclinA2}$ structure [6] (PDB: 6Q6H, EMDB: 4466), reveals cryo-EM density corresponding to the CDC20 N-terminal α-helix (**Fig. 2e**). Compared to CDH1$^{\alpha1}$ of the APC/C$^{CDH1:EMI1}$ ternary complex, CDC20$^{\alpha1}$ is shorter, and density corresponding to CDC20$^{\alpha1}$ is less well defined, possibly indicating lower occupancy, although we note the lower resolution of the APC/C$^{CDC20:CyclinA2}$ map may contribute to this less well defined cryo-EM density.

The position of CDH1$^{\alpha1}$ abuts the anchor points of the long 300s loop of APC1 (APC1^{300s}) that is inserted within APC1^{WD40} (**Fig. 2b**). The tip of APC1^{300s} comprises the APC1 auto-inhibitory segment (APC1^{AI}) that in the unphosphorylated APC/C binds the C-box recognition site of APC8, thereby inhibiting CDC20, but not CDH1, binding to the APC/C [8,11]. As reported previously [8,11,12], phosphorylation of APC1^{300s} removes APC1^{AI} from the C-box recognition site, allowing CDC20 to bind. It seems likely that phosphorylation of APC1, whilst releasing APC1^{AI} from the C-box binding site, would also displace the APC1^{300s} anchor points, facilitating α1-helix binding. Indeed, comparing the new 3.2 Å resolution unphosphorylated apo-APC/C structure determined in this study (discussed below) with APC/C$^{CDH1:EMI1}$ shows that CDH1$^{\alpha1}$ overlaps with the C-terminal region of APC1^{300s} (residues 400-402) as observed in the apo state of APC/C. When bound to CDH1, this loop segment is pushed upwards towards APC8 (**Fig. 2c**).

CDH1$^{\alpha1}$ is a few residues longer than CDC20$^{\alpha1}$ (**Fig. 2d, e**) offering additional contact sites with APC1. Thus, phosphorylation of APC1^{300s} by CDK1/2 remodels APC1^{300s} both to remove APC1^{AI} from the C box-binding site in APC8(B), and to remove a steric obstacle to the binding of the coactivator α1 helix to APC1^{WD40}. The larger interface formed between CDH1$^{\alpha1}$ and APC1^{WD40} compared with CDC20$^{\alpha1}$ might contribute to the enhanced affinity of CDH1 for unphosphorylated APC/C relative to CDC20. We showed previously that differences between CDH1 and CDC20 in both their N-terminal domains and IR tails contribute to the higher affinity of CDH1 for unphosphorylated APC/C [8].

2. **Zinc-binding module in APC2 (APC2^{ZBM}).** An important insight from the new maps is the discovery of a zinc-binding module in cullin repeat 2 (CR2) of APC2 (APC2^{ZBM}). The new cryo-EM density, aided by an AlphaFold model of human APC2, allowed a partially built region of APC2 in PDB 4ui9 to be modelled (residues 187-233, **Supplementary Table 2**) (**Fig. 3a-c**). This segment constitutes a 45-residue insert between the A and B α-helices of cullin repeat 2. The insert comprises a 15-residue loop and an exposed α-helix (helix-AB, **Fig. 3b**), followed by a β-hairpin loop that abuts the N-terminus of the adjoining α-helix B. Four cysteine residues, two from the β-hairpin (Cys221 and Cys224), and two from the distorted N-terminus of α-helix B (Cys231 and Cys233), coordinate a metal ion organized with tetrahedral geometry. The sulphur-metal ion distances measure 2.3 Å on average, typical of sulphur-metal coordination bond lengths. To identify the metal composition, we subjected the APC2:APC11 heterodimer to proton-induced X-ray emission spectroscopy (PIXE) [13]. This revealed APC2:APC11 to contain zinc ions, with no other metal ions. Human APC11 contains three zinc-binding sites. Calibration of the Zn:S stoichiometry indicated 2.5 zinc ions bound to APC2:APC11, less than the four expected assuming a zinc-binding site in APC2 (**Supplementary Table 3**). However, mutation of the four Cys residues (C221, C224, C231, C233) of the metal-binding site of APC2 decreased the zinc content by one zinc atom, consistent with the assignment of the metal-binding site in APC2 as a novel Cys-dependent zinc-binding site. We assume the sub-stoichiometric Zn content of APC2:APC11 results from partial occupancy of APC11 Zn-sites.

Multiple sequence alignments indicate absolute conservation of APC2^{ZBM}, as defined by the four zinc-coordinating Cys residues within metazoan APC2 sequences (from humans to *C. elegans*) (**Fig. 3d**), with no Cys conservation in budding yeast (data not shown), consistent with the absence of a zinc-module in APC2 of the *S. cerevisiae* APC/C cryo-EM structure (PDB: 8A3T; E. Vazquez-Fernandez, D. Barford *et al*., unpublished). The presence of APC2^{ZBM} correlates well with the conservation of the coactivator N-terminal α-helix in metazoan APC/C coactivator subunits (**Fig. 2f, g and Fig. 3d**). The configuration of the four zinc-coordinating Cys residues of APC2^{ZBM} is highly reminiscent of the zinc finger motifs of

classical zinc-containing DNA-binding domains first observed in the oestrogen receptor [14], and also related to the Cys and His containing zinc fingers typified by the transcription factor TFIIIA [15]. In these proteins two Cys residues, three residues apart in a loop, together with two Cys (oestrogen receptor) or His residues (TFIIIA) of an adjoining C-terminal α-helix, coordinate a zinc ion.

Role of zinc-binding module.
(i) Effects of mutating APC2^{ZBM} on APC/C E3 ligase activity. To determine the role of APC2^{ZBM}, we assessed the consequence of mutating the four zinc-coordinating Cys residues to alanines on the APC/C ubiquitination activity. We found that the ubiquitination activity of APC/C, using UbcH10, with the mutant APC2^{ZBM} was not impaired relative to wild type APC/C. This result is consistent with the APC2^{ZBM} and the UbcH10-binding site, at the combined interface of APC2^{WHB}:APC11^{RING}, being separated by over 100 Å.

(ii) Effects of mutating APC2^{ZBM} on SUMOylation of APC/C. APC2^{ZBM} is positioned facing towards the APC4 WD40 domain (APC4^{WD40}), proximal to the C-terminus of APC4. Residues 759-808 of APC4, including the two sites of SUMOylation Lys772 and Lys798 [16] are disordered in the APC/C cryo-EM maps. We considered the possibility that APC2^{ZBM} may contribute to a binding interface for UBC9, the E2 responsible for APC/C SUMOylation [16]. We assessed the consequence of mutating APC2^{ZBM} on the efficacy of APC4 SUMOylation. Compared to wild type APC/C, APC/C with a mutated APC2^{ZBM} showed no reduction in APC4 SUMOylation. From this result, we conclude that the APC2^{ZBM} does not contribute to UBC9 recognition by the APC/C. Furthermore, APC2^{ZBM} is remote (>40 Å) from the SUMO and APC2^{WHB} binding sites at the APC2:APC4 interface [16,17], suggesting that APC2^{ZBM} likely does not directly mediate SUMO and APC2^{WHB} binding to the APC/C. Whether the zinc-finger motif in APC2 plays a role in APC/C activity under physiological conditions will require future studies.

3. **Extension of APC6 C-terminus (APC6^{CT}).** In our previous structure (PDB 4ui9), we built an extended region of a chain that transverses the APC1:APC2 subunit interface. The absence of well-resolved side-chain density prevented subunit assignment, although the proximity of one end of this segment to the C-terminal TPR helix of APC6(A) suggested it may correspond to the low-complexity C-terminal region of APC6. In the new map, clearly defined side-chain density allows assignment to the C-terminal region of APC6(A) (APC6^{CT}) (**Fig. 1d and Fig. 4a-c**). Thus, this demonstrates one of the key and reoccurring functions of low complexity/intrinsically disordered regions present in numerous APC/C subunits, that is, to stabilize inter-subunit interactions through a staple-like mechanism. The equivalent region (residues 544 to 567) is disordered in the second APC6 subunit of the APC6 homo-dimer APC6(B).

   In our studies thus far [7,18] we highlighted the role of the IDRs of the small APC/C subunits APC12, APC13, APC15 and APC16 in forming extended structures that bridge inter-subunit interfaces. APC6^{CT} together with an internal loop of β-blade1 of APC1^{WD40} (residues 35-69) that interacts with APC8(B), exemplify the role of IDRs of larger globular proteins in stabilizing inter-subunit interactions (**Fig. 5**).

4. **KEN box of EMI1 bound to the CDH1 KEN-binding site.** EMI1 inhibits the APC/C through three mechanisms: (i) blockade of the D-box co-receptor through a pseudo-substrate D-box sequence in EMI1 (residues 322 to 330); (ii) steric hindrance of UBCH10 binding to the RING domain of APC11, mediated by EMI1^{ZBR}, and (iii) through its C-terminal LRRL motif, identical to the C-terminus of UBE2S [19], EMI1 competes with UBE2S for the LRRL-binding site on APC2, required by UBE2S to bind APC/C [7,20-22] (**Fig. 1c and Fig. 6a**). In our new maps we

noticed cryo-EM density adjacent to the KEN box-binding site of CDH1^{WD40} (**Fig. 6b**). This density matched closely with the crystal structure of the KEN-box of *S. cerevisiae* ACM1 at the *S. cerevisiae* CDH1^{WD40} (PDB: 4BH6) [23]. Aoded by an AlphaFold prediction (**Supplementary Fig. 3**), we fitted residues 113 to 123 of EMI1 to this density (**Fig. 6a, b**). Residues of the 'NKEN' sequence of EMI1 conform to a consensus KEN motif sequence [23], and interact with CDH1^{WD40}. Previous studies however showed that the N-terminal region of EMI1 (residues 1-244) is unable in itself to bind APC/C^{CDH1}, in contrast to the C-terminal segment of residues 299-447 [22]. We propose that the EMI1^{KEN} motif, by binding to CDH1^{WD40}, both enhances the affinity of EMI1 for APC/C^{CDH1} concomitantly with occlusion of the KEN-box receptor on CDH1, thereby blocking KEN-box dependent substrates from binding the APC/C. Finally, our new maps also resulted in an improved model of the C-terminal LRRL motif of EMI1 at the APC2:APC4 interface (**Fig. 6a**).

Apo-APC/C

Cryo-EM 3D classification revealed two apo APC/C classes, representing 28% of the total selected APC/C particles (**Supplementary Fig. 2 and Supplementary Table 1**). Apo-APC/C was reconstructed to a resolution of 3.2 Å and rebuilt based on the revised 2.9 Å APC/C$^{CDH1:EMI1}$ structure (**Fig. 7)**. As expected, as for APC/C$^{CDH1:EMI1}$, we observe the zinc-binding module in APC2. Major remodelling involved regions of APC/C that undergo conformational change on conversion from apo-APC/C to the ternary state, promoted by CDH1 binding [18]. These regions comprise the catalytic platform of APC2 and adjacent subunits APC1, APC4, APC5 and APC8(B). The conformational differences between APC/C$^{CDH1:EMI1}$ and apo-APC/C involve the downwards movement of the APC2:APC11 module bringing the catalytic module (APC2^{CTD}:APC11) to a position close to APC4:APC5 that blocks binding of the ubiquitin-charged UBCH10 to APC2^{CTD}:APC11 [7]. The conformational change to the active state is induced by the N-terminal domain of CDH1 (CDH1^{NTD}) interacting with the proteosome-cyclosome (PC) domain of APC1 (APC1^{PC}). In the ternary complex, CDH1^{NTD} disrupts the interaction between APC1^{PC} and APC8(B) by binding to a site on APC1^{PC} that overlaps the site in contact with APC8(B). This wedges APC1^{PC} and APC8(B) apart and disorders TPR motifs 13 and 14 of APC8(B). A concomitant downwards-displacement of APC8(B) tilts the platform to translate the APC2^{CTD}:APC11 module upwards (**Supplementary Video 1**).

With the new apo-APC/C map, we re-examined the structure of the APC1^{AI}, also aided by an AlphaFold prediction of a model of APC8 with residues 201-400 of APC1 (**Supplementary Fig. 4**). The AlphaFold run generated a model, scored with high confidence, predicting that residues 345 to 357 of APC1 dock as an α-helix into APC8$^{C\text{-}box}$. Leu350 and Arg352 of APC1 are well defined in density (**Fig. 8a-c**), with the Arg and Leu mimicking the conserved Arg and Ile of the C-box motif (DR^{47}[F/Y]I^{49}PxR) (**Fig. 8d**). Ser351 and Ser355 of APC1, sites of mitotic phosphorylation [24-26], and *in vitro* phosphorylation by CDK2-cyclinA3 [8], are located within this AI segment. Phosphorylation of either serine would not be compatible with APC1^{A1} binding to APC8$^{C\text{-}box}$, suggesting a mechanism by which APC1 phosphorylation relieves APC8$^{C\text{-}box}$ inhibition by APC1^{AI}, thereby allowing CDC20 binding (**Fig. 8b inset**). Ser355 is within cluster-5 of serine residues (S355, S362, S372, S377) that when mutated to glutamate, promote APC/C^{CDC20} activation [11].

<u>Conclusions</u>

Our previous 3.6 Å resolution map of the APC/C$^{CDH1:EMI1}$ complex was determined in 2014 [7], during the early period of the cryo-EM resolution revolution [27]. The cryo-EM data were collected on a Polara microscope fitted with the first generation of direct electron detectors (FEI Falcon 2). Our new structures reported here benefit from advances in both cryo-EM hardware (Titan Krios electron microscopes with a more coherent and parallel electron beam), and direct electron detectors with improved detector quantum efficiency (DQE) and data collection rates, coupled to energy filters.

These hardware developments have been combined with improvements in data processing analysis in RELION [28] and cryoSPARC [29], allowing the segmentation of flexible large complexes into rigid body domains, combined with signal subtraction methods, for independent alignment, 3D classification and refinement of discrete structural units. Last, the huge advances in the accuracy and reliability of protein structure prediction achieved through AlphaFold [9,10] and RoseTTAFold [30], allow the interpretation of difficult-to-build regions of cryo-EM maps. Altogether these developments have resulted in new insights into APC/C structure and function including (i) definition of the N-terminal α-helix of CDH1, (ii) definition at the residue level of previously unbuilt low complexity regions (formed from IDRs), for example the APC6 C-terminus (**Supplementary Table 4**), (iii) definition of the Zn-binding module of APC2, and (iv) discovery of the pseudo-substrate KEN motif of EMI1 that blocks the KEN-box binding site of CDH1, contributing to EMI1-mediated inhibition of APC/C^{CDH1}.

Materials and Methods

Sample Preparation and data collection

The APC/C$^{CDH1:EMI1}$ ternary complex and cryo-EM grids were prepared as described previously [7]. Data collection was performed on Krios TEMs equipped with Falcon 3 detectors (ThermoFisherScientific). Details in **Supplementary Table 1**.

Cloning and expression of wild type and mutant APC2:APC11 complexes

Wild type APC2:APC11 with an N-terminal double StrepII-tag on APC2 was cloned into the baculovirus expression system and expressed using the methods described previously [31]. The mutant APC2:APC11 complex was generated by substituting Ala for Cys221, Cys224, Cys231 and Cys233 of APC2. Wild type APC2:APC11 and mutant complexes were expressed in Hi5 cells. The lysate was loaded onto three tandemly linked Strep-Tactin columns (Qiagen) and the complexes were eluted with 2.5 mM desthiobiotin (Sigma) in a buffer of 50 mM Tris.HCl (pH 8.0), 200 mM NaCl, 1 mM DTT. The elution was treated with C-terminal tobacco etch virus (TEV) protease at 4°C overnight to cleave the double StrepII-tag. The complexes were further purified using Resource Q anion-exchange and size exclusion chromatography (Superdex S200 column) (Cytiva) in a buffer of 20 mM Hepes (pH 8.0), 200 mM NaCl, 2 mM DTT.

Proton-induced X-ray emission (PIXE) experiments

Wild type and mutant APC2:APC11 complexes were dialysed for 16 h at 4 °C against a chloride-free buffer of 50 mM Tris.acetate (pH 7.5) and 200 mM sodium acetate (pH adjusted using acetic acid) and concentrated to 1.6 mg/mL (wild type) and 2.5 mg/mL (APC2:APC11 mutant). The PIXE experiment was perfomed at the Ion Beam Centre, University of Surrey, using methods described in [13,32].

Image Processing

Image processing was performed in cryoSPARC v.3.3.1 [29] and RELION 3.1 [28]. A detailed processing pipeline can be found in **Supplementary Fig. 2**. In summary, movies in two separate data sets (a total of 8296 movies) were motion corrected using MotionCor2 [33] (implemented in RELION) and dose-weighted micrographs were imported into cryoSPARC to perform the contrast transfer function (CTF) parameter estimation using patch-based CTF estimation. Particles were first manually picked on a small subset of micrographs. This particle set was used to train a Topaz model for automated particle picking [34], which was then applied to the entire data set. Particles were cleaned through two rounds of 2D classification. A first *ab initio* reconstruction with four classes was generated and a subsequent heterogenous 3D refinement was performed. Good classes of particles were selected and subjected to non-uniform refinement combined with CTF refinement. The resolution was further improved by Bayesian polishing in RELION. After the polishing step the resulting particles from the two independent data sets were combined and re-imported into cryoSPARC for another round of 3D classification using eight classes. This allowed efficient separation of APC/C particles in the apo state

from the APC/C$^{CDH1:EMI1}$ particles. Selected particles were used for a final 3D non-uniform refinement and CTF refinement run. Local refinements were performed by applying soft masks on the catalytic domain (Mask 1), on the TPR lobe of APC/C (Mask 2), and the central region containing the APC8 tail as well as CDH1 (Mask 3), respectively. For the latter two, particle subtraction had been performed prior to local refinement. All final maps have been sharpened using deepEMhancer [35]. Final resolution estimation was calculated using gold-standard Fourier Shell Correlation (FSC) based on two independent half maps, and applying the 0.143 criterion [36].

Model Building

Model building of the APC/C$^{CDH1:EMI1}$ ternary complex was performed using COOT [37]. The available structure of APC/C$^{CDH1:EMI1}$ (PDB: 4UI9) [7] was first fitted into the cryo-EM maps in Chimera [38] as an initial model. The model was rebuilt manually based on the new cryo-EM density. Previously undefined regions were built *ab initio* into the densities. Modelling of difficult to interpret regions of the maps were aided using AlphaFold predictions [9,10]. Model building of the apo-APC/C structure was performed identically to the APC/C$^{CDH1:EMI1}$ structure, using the available structure (PDB: 5G05) as initial model. The Alphafold prediction was fitted into the density and refined manually using COOT. Real-space refinement was performed in PHENIX [39] and the refined model was validated using the MolProbity tool [40]. Maps and models were visualized, and figures generated, using Chimera X [41]. Multiple sequence alignments were displayed using JalView2 [42].

AlphaFold Predictions

AlphaFold2 [9] predictions were performed locally. For the APC1^{AI}:APC8 model, residues 201 to 400 of APC1 and full-length APC8 were used. The Alphafold prediction was fitted into the density and refined manually using COOT. For the CDH1^{WD40}:EMI1$^{KEN\text{-}box}$ model, full length sequences of CDH1 and EMI1 were used.

Acknowledgements

We are grateful to the LMB EM Facility for help with the EM data collection, J. Grimmett and T. Darling for computing, and J. Shi for help with insect cell expression. For the purpose of open access, the author has applied a CC BY public copyright license to any Author Accepted Manuscript version arising.

Funding

This work was supported by grants of the Swiss National Science Foundation (310030_185235 and TMSGI3_211581) and the Swiss Cancer League (KFS-5453-08-2021) (A.B.) and by UKRI/Medical Research Council MC_UP_1201/6 (D.B.) and Cancer Research UK C576/A14109 (D.B.).

Competing interests

Authors declare that they have no competing interests.

Data and materials availability

PDB and cryo-EM maps have been deposited with RCSB and EMDB, respectively. Accession numbers are listed in Supplementary Table 1.

Author contributions

The project has been conceived by D.B, A.B. and L.C.
Experiments were performed by A.H., J.Yu, J.Y., Z.Z., L.C., G.W.G., E.F.G., A.B., D.B.
The paper was written by D.B., A.B., A.H., J.Yu, with input from all other authors.

Supplementary Video

Video shows conformational change on transition from apo-APC/C to the APC/C$^{CDH1:EMI1}$ ternary complex. Apo-APC/C and APC/C$^{CDH1:EMI1}$ were superimposed on APC1^{PC}.

References

1 Alfieri, C., Zhang, S. & Barford, D. Visualizing the complex functions and mechanisms of the anaphase promoting complex/cyclosome (APC/C). *Open biology* **7**, doi:10.1098/rsob.170204 (2017).

2 Barford, D. Structural interconversions of the anaphase-promoting complex/cyclosome (APC/C) regulate cell cycle transitions. *Current opinion in structural biology* **61**, 86-97, doi:10.1016/j.sbi.2019.11.010 (2020).

3 Watson, E. R., Brown, N. G., Peters, J. M., Stark, H. & Schulman, B. A. Posing the APC/C E3 Ubiquitin Ligase to Orchestrate Cell Division. *Trends in cell biology* **29**, 117-134, doi:10.1016/j.tcb.2018.09.007 (2019).

4 Bodrug, T., Welsh, K. A., Hinkle, M., Emanuele, M. J. & Brown, N. G. Intricate Regulatory Mechanisms of the Anaphase-Promoting Complex/Cyclosome and Its Role in Chromatin Regulation. *Front Cell Dev Biol* **9**, 687515, doi:10.3389/fcell.2021.687515 (2021).

5 Yu, J., Morgan, D. O. & Boland, A. The molecular mechanisms of human separase regulation. *Biochemical Society transactions* **51**, 1225-1233, doi:10.1042/BST20221400 (2023).

6 Zhang, S., Tischer, T. & Barford, D. Cyclin A2 degradation during the spindle assembly checkpoint requires multiple binding modes to the APC/C. *Nature communications* **10**, 3863, doi:10.1038/s41467-019-11833-2 (2019).

7 Chang, L., Zhang, Z., Yang, J., McLaughlin, S. H. & Barford, D. Atomic structure of the APC/C and its mechanism of protein ubiquitination. *Nature* **522**, 450-454, doi:10.1038/nature14471 (2015).

8 Zhang, S. *et al.* Molecular mechanism of APC/C activation by mitotic phosphorylation. *Nature* **533**, 260-264, doi:10.1038/nature17973 (2016).

9 Jumper, J. *et al.* Highly accurate protein structure prediction with AlphaFold. *Nature*, doi:10.1038/s41586-021-03819-2 (2021).

10 Tunyasuvunakool, K. *et al.* Highly accurate protein structure prediction for the human proteome. *Nature*, doi:10.1038/s41586-021-03828-1 (2021).

11 Qiao, R. *et al.* Mechanism of APC/CCDC20 activation by mitotic phosphorylation. *Proceedings of the National Academy of Sciences of the United States of America* **113**, E2570-2578, doi:10.1073/pnas.1604929113 (2016).

12 Fujimitsu, K., Grimaldi, M. & Yamano, H. Cyclin-dependent kinase 1-dependent activation of APC/C ubiquitin ligase. *Science* **352**, 1121-1124, doi:10.1126/science.aad3925 (2016).

13 Grime, G. W. *et al.* High-Throughput PIXE as an Essential Quantitative Assay for Accurate Metalloprotein Structural Analysis: Development and Application. *J Am Chem Soc* **142**, 185-197, doi:10.1021/jacs.9b09186 (2020).

14 Schwabe, J. W., Neuhaus, D. & Rhodes, D. Solution structure of the DNA-binding domain of the oestrogen receptor. *Nature* **348**, 458-461, doi:10.1038/348458a0 (1990).

15 Lee, M. S., Gippert, G. P., Soman, K. V., Case, D. A. & Wright, P. E. Three-dimensional solution structure of a single zinc finger DNA-binding domain. *Science* **245**, 635-637, doi:10.1126/science.2503871 (1989).

16 Yatskevich, S. *et al.* Molecular mechanisms of APC/C release from spindle assembly checkpoint inhibition by APC/C SUMOylation. *Cell reports* **34**, 108929, doi:10.1016/j.celrep.2021.108929 (2021).

17 Alfieri, C., Tischer, T. & Barford, D. A unique binding mode of Nek2A to the APC/C allows its ubiquitination during prometaphase. *EMBO reports* **21**, e49831, doi:10.15252/embr.201949831 (2020).

18 Chang, L., Zhang, Z., Yang, J., McLaughlin, S. H. & Barford, D. Molecular architecture and mechanism of the anaphase-promoting complex. *Nature* **513**, 388-393, doi:10.1038/nature13543 (2014).

19 Meyer, H. J. & Rape, M. Enhanced protein degradation by branched ubiquitin chains. *Cell* **157**, 910-921, doi:10.1016/j.cell.2014.03.037 (2014).

20 Frye, J. J. *et al.* Electron microscopy structure of human APC/C(CDH1)-EMI1 reveals multimodal mechanism of E3 ligase shutdown. *Nature structural & molecular biology* **20**, 827-835, doi:10.1038/nsmb.2593 (2013).

21 Wang, W. & Kirschner, M. W. Emi1 preferentially inhibits ubiquitin chain elongation by the anaphase-promoting complex. *Nature cell biology* **15**, 797-806, doi:10.1038/ncb2755 (2013).

22 Miller, J. J. *et al.* Emi1 stably binds and inhibits the anaphase-promoting complex/cyclosome as a pseudosubstrate inhibitor. *Genes & development* **20**, 2410-2420 (2006).
23 He, J. *et al.* Insights into Degron Recognition by APC/C Coactivators from the Structure of an Acm1-Cdh1 Complex. *Molecular cell* **50**, 649-660, doi:S1097-2765(13)00329-8 [pii] 10.1016/j.molcel.2013.04.024 (2013).
24 Kraft, C. *et al.* Mitotic regulation of the human anaphase-promoting complex by phosphorylation. *The EMBO journal* **22**, 6598-6609 (2003).
25 Steen, J. A. *et al.* Different phosphorylation states of the anaphase promoting complex in response to antimitotic drugs: a quantitative proteomic analysis. *Proceedings of the National Academy of Sciences of the United States of America* **105**, 6069-6074 (2008).
26 Hegemann, B. *et al.* Systematic phosphorylation analysis of human mitotic protein complexes. *Science signaling* **4**, rs12, doi:10.1126/scisignal.2001993 (2011).
27 Kuhlbrandt, W. Biochemistry. The resolution revolution. *Science* **343**, 1443-1444, doi:10.1126/science.1251652 (2014).
28 Zivanov, J. *et al.* New tools for automated high-resolution cryo-EM structure determination in RELION-3. *eLife* **7**, doi:10.7554/eLife.42166 (2018).
29 Punjani, A., Rubinstein, J. L., Fleet, D. J. & Brubaker, M. A. cryoSPARC: algorithms for rapid unsupervised cryo-EM structure determination. *Nat Methods* **14**, 290-296, doi:10.1038/nmeth.4169 (2017).
30 Baek, M. *et al.* Accurate prediction of protein structures and interactions using a three-track neural network. *Science* **373**, 871-876, doi:10.1126/science.abj8754 (2021).
31 Zhang, Z., Yang, J. & Barford, D. Recombinant expression and reconstitution of multiprotein complexes by the USER cloning method in the insect cell-baculovirus expression system. *Methods* **95**, 13-25, doi:10.1016/j.ymeth.2015.10.003 (2016).
32 Grime, G. W. & Garman, E. F. The identification and quantification of metal atoms in proteins using microPIXE: a critical evaluation. *Nuclear Instruments and Methods in Physics Research Section B: Beam Interactions with Materials and Atoms* **540**, 237-245, doi:doi.org/10.1016/j.nimb.2023.03.025 (2023).
33 Zheng, S. Q. *et al.* MotionCor2: anisotropic correction of beam-induced motion for improved cryo-electron microscopy. *Nat Methods* **14**, 331-332, doi:10.1038/nmeth.4193 (2017).
34 Bepler, T. *et al.* Positive-unlabeled convolutional neural networks for particle picking in cryo-electron micrographs. *Nat Methods* **16**, 1153-1160, doi:10.1038/s41592-019-0575-8 (2019).
35 Sanchez-Garcia, R. *et al.* DeepEMhancer: a deep learning solution for cryo-EM volume post-processing. *Commun Biol* **4**, 874, doi:10.1038/s42003-021-02399-1 (2021).
36 Rosenthal, P. B. & Henderson, R. Optimal determination of particle orientation, absolute hand, and contrast loss in single-particle electron cryomicroscopy. *Journal of molecular biology* **333**, 721-745, doi:10.1016/j.jmb.2003.07.013 (2003).
37 Emsley, P. & Cowtan, K. Coot: model-building tools for molecular graphics. *Acta crystallographica. Section D, Biological crystallography* **60**, 2126-2132 (2004).
38 Yang, Z. *et al.* UCSF Chimera, MODELLER, and IMP: an integrated modeling system. *Journal of structural biology* **179**, 269-278, doi:S1047-8477(11)00261-9 [pii] 10.1016/j.jsb.2011.09.006 (2012).
39 Adams, P. D. *et al.* PHENIX: a comprehensive Python-based system for macromolecular structure solution. *Acta crystallographica. Section D, Biological crystallography* **66**, 213-221, doi:10.1107/S0907444909052925 (2010).
40 Williams, C. J. *et al.* MolProbity: More and better reference data for improved all-atom structure validation. *Protein science : a publication of the Protein Society* **27**, 293-315, doi:10.1002/pro.3330 (2018).
41 Goddard, T. D. *et al.* UCSF ChimeraX: Meeting modern challenges in visualization and analysis. *Protein science : a publication of the Protein Society* **27**, 14-25, doi:10.1002/pro.3235 (2018).
42 Waterhouse, A. M., Procter, J. B., Martin, D. M., Clamp, M. & Barton, G. J. Jalview Version 2--a multiple sequence alignment editor and analysis workbench. *Bioinformatics* **25**, 1189-1191, doi:10.1093/bioinformatics/btp033 (2009).

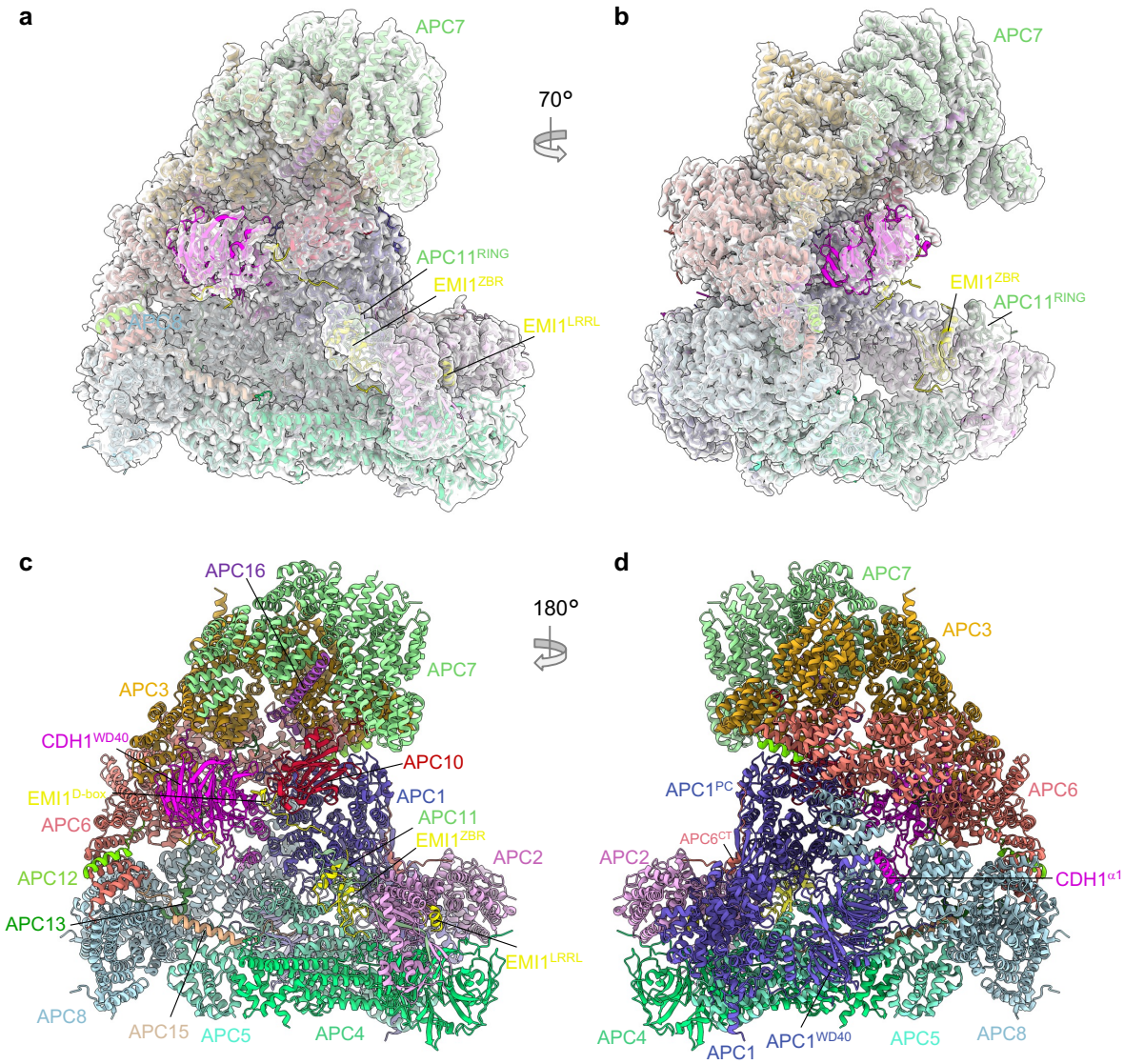

Figure 1. Overall structure of the APC/C$^{CDH1:EMI1}$ complex. a, and **b**, Two views of the APC/C$^{CDH1:EMI1}$ ternary complex fitted into the 2.9 Å cryo-EM map. **c**, and **d**, Two views of the APC/C$^{CDH1:EMI1}$ ternary complex shown as ribbons representations.

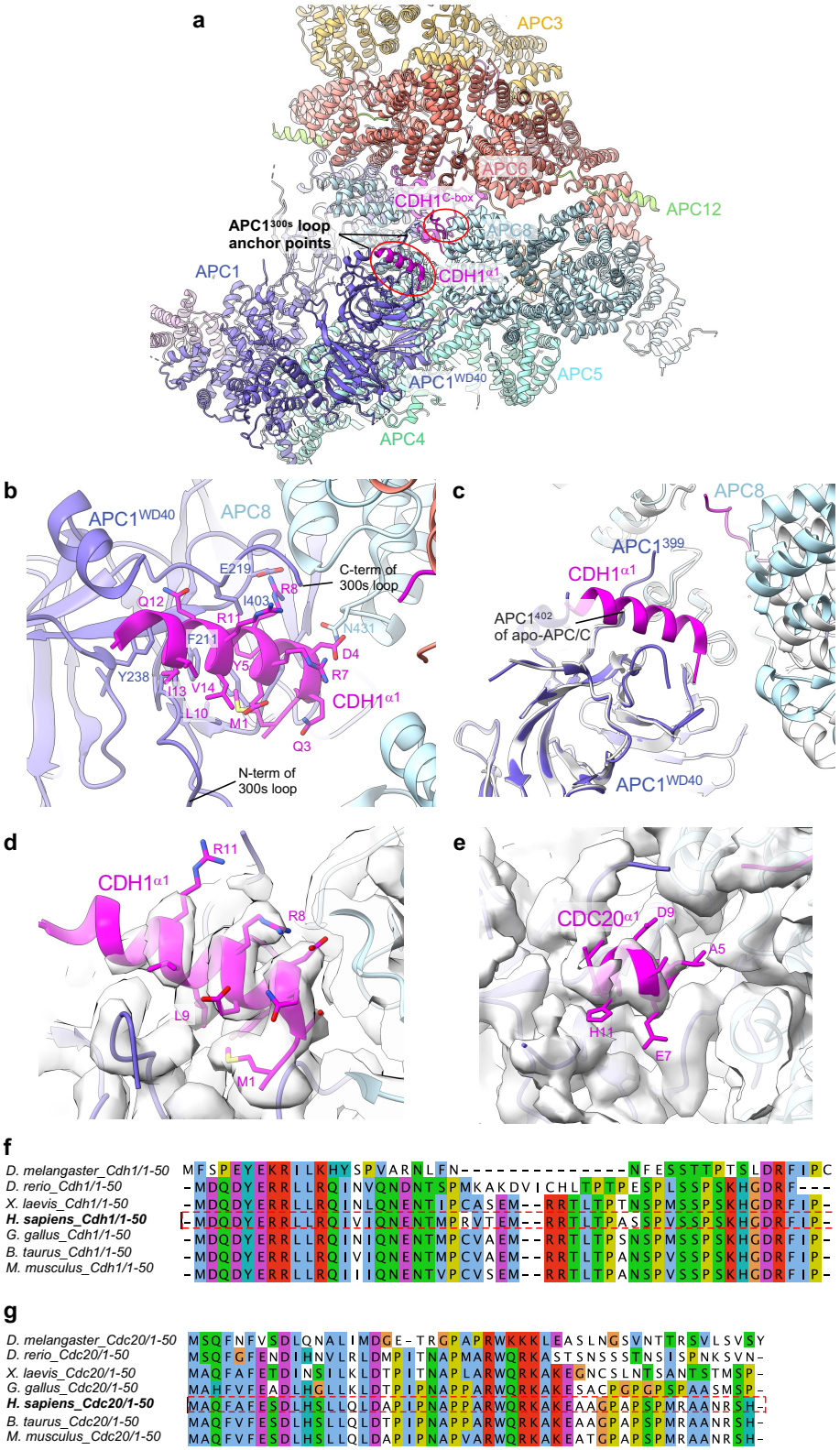

Figure 2. Details of CDH1$^{\alpha1}$ interaction with APC1^{WD40}. **a**, Overview of CDH1$^{\alpha1}$:APC1^{WD40} interactions. **b**, Detailed view of CDH1$^{\alpha1}$ interacting with APC1^{WD40}. **c**, Superimposition of APC/C$^{CDH1:EMI1}$ onto apo-APC/C showing how CDH1$^{\alpha1}$ overlaps with the C-terminal region of the APC1^{300s} loop of apo-APC/C (coloured light grey). **d**, Cruo-EM density map showing CDH1$^{\alpha1}$. **e**, An equivalent, although shorter N-terminal α-helix exists in CDC20. Map of CDC20$^{\alpha1}$:APC1^{WD40} interactions (from EMDB: 4466) [6]. **f**, Multiple sequence alignments showing conservation of metazoan CDH1$^{\alpha1}$ and (**g**) CDC20$^{\alpha1}$.

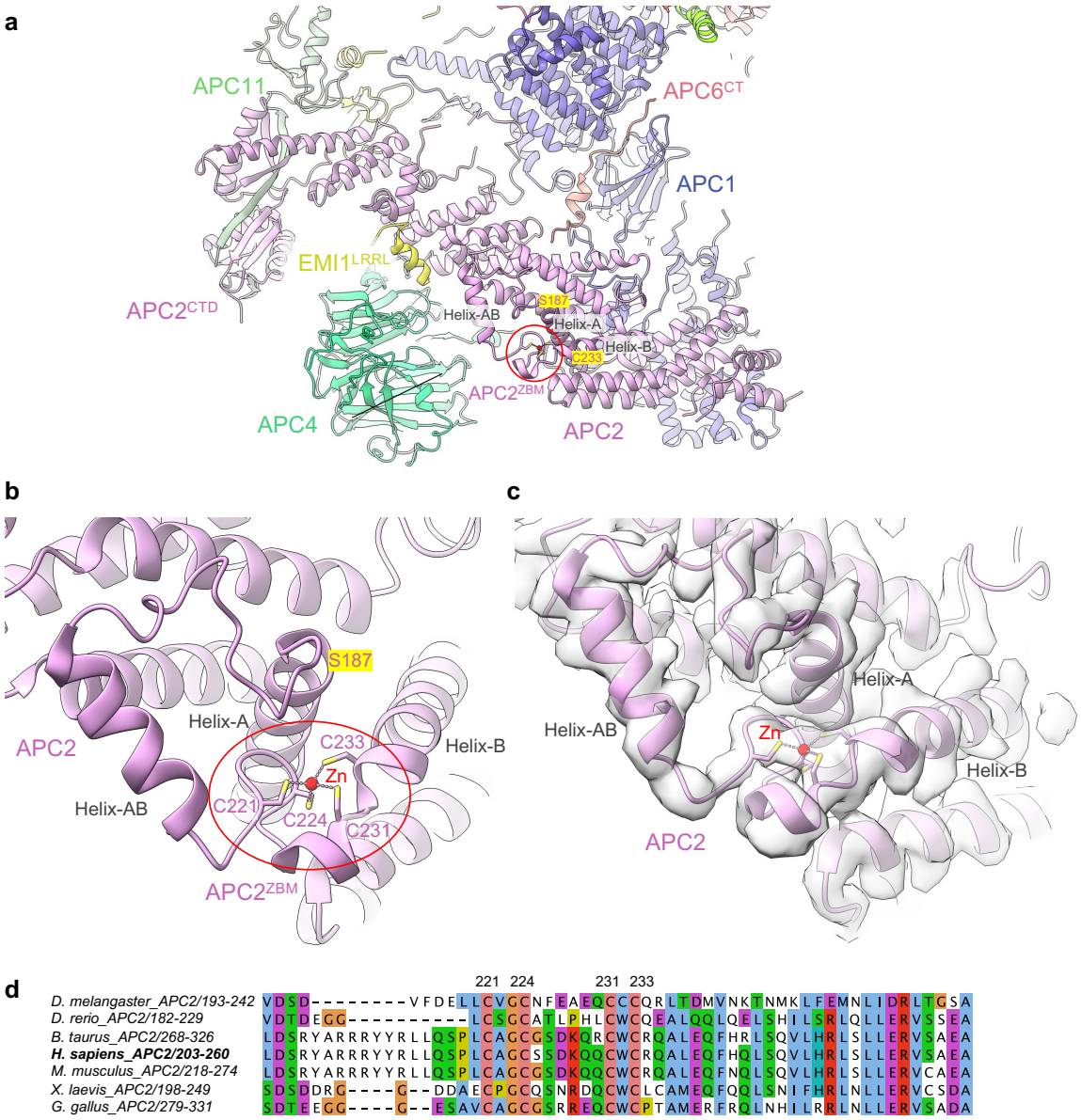

Figure 3. Zn-binding motif of APC2 (APC2^{ZBM}). a, Overview view showing APC2^{ZBM}. **b**, Details of the APC2^{ZBM}. **C**, Cryo-EM density map of APC2^{ZBM}. **c**, MSA of metazoan APC2 showing conservation of the APC2^{ZBM}.

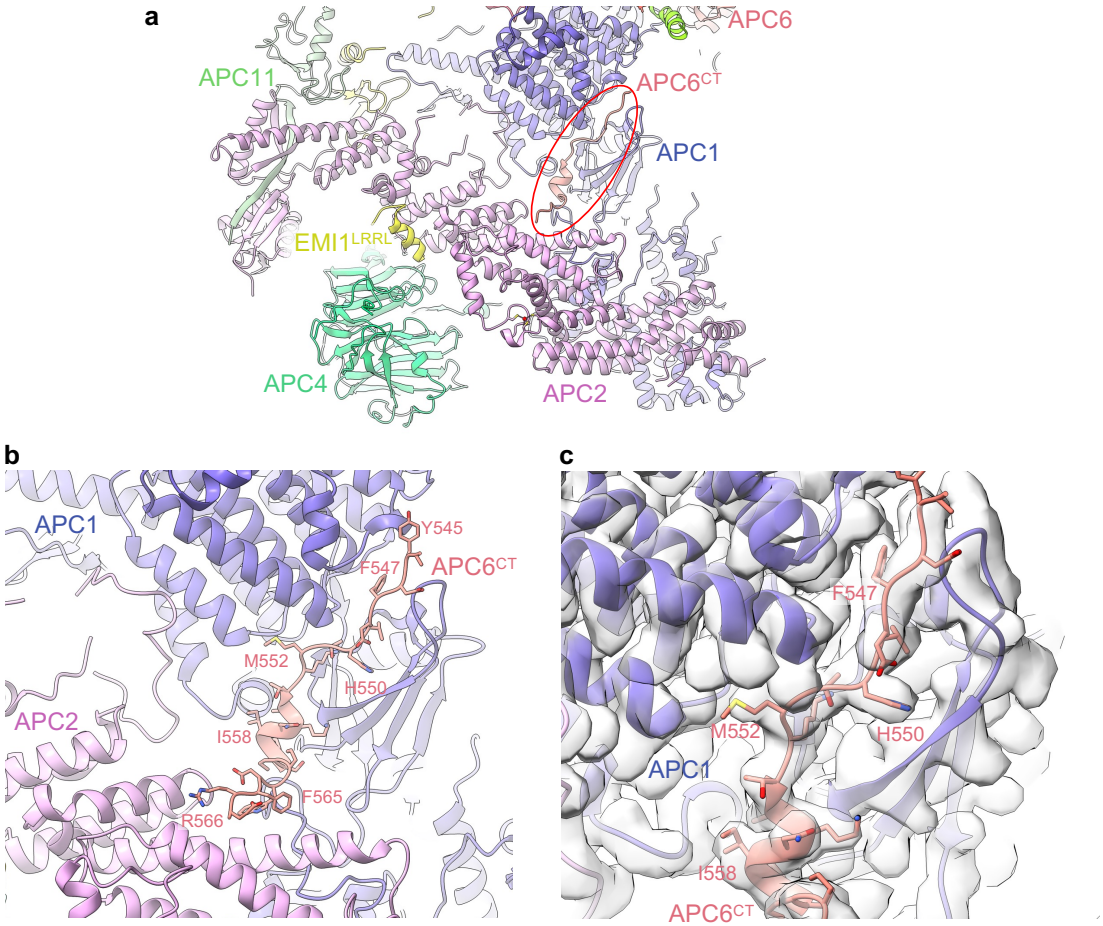

Figure 4. APC6^{CT} - APC1:APC2 inter-connector. a, Overview figure showing APC6^{CT} inter-connector linking the APC1:APC2 interface. **b**, Details of the APC6^{CT} APC1-APC2 inter-connector. **c**, Cryo-EM density map of the APC6^{CT} APC1:APC2 inter-connector.

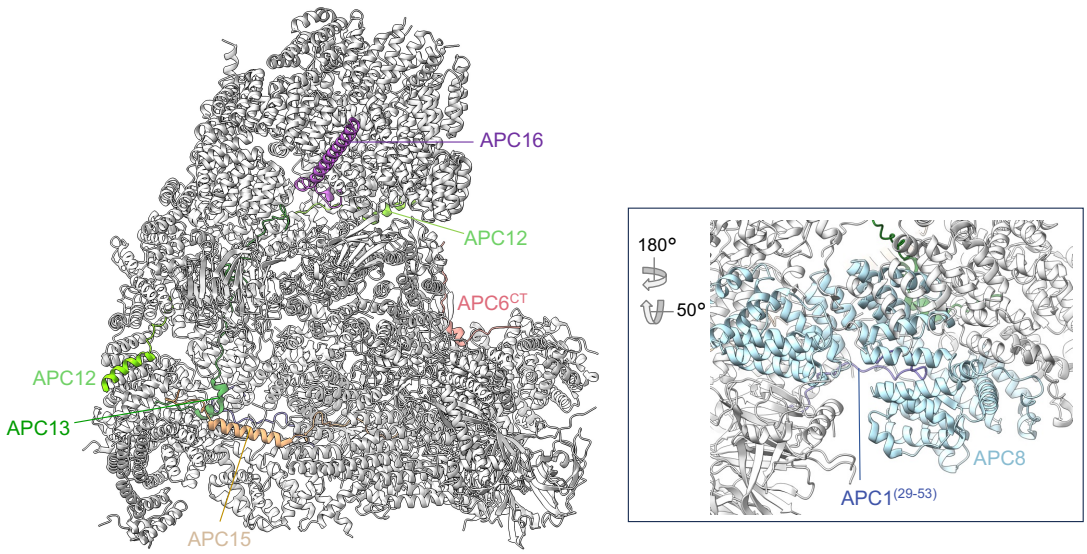

Figure 5. IDRs function to inter-connect APC/C subunits. Shown coloured are: APC6^{CT} (residues 544-567), Apc12, Apc13, Apc15, Apc16. Inset: APC1 (residues 29-53) interacting within the TPR groove of APC8.

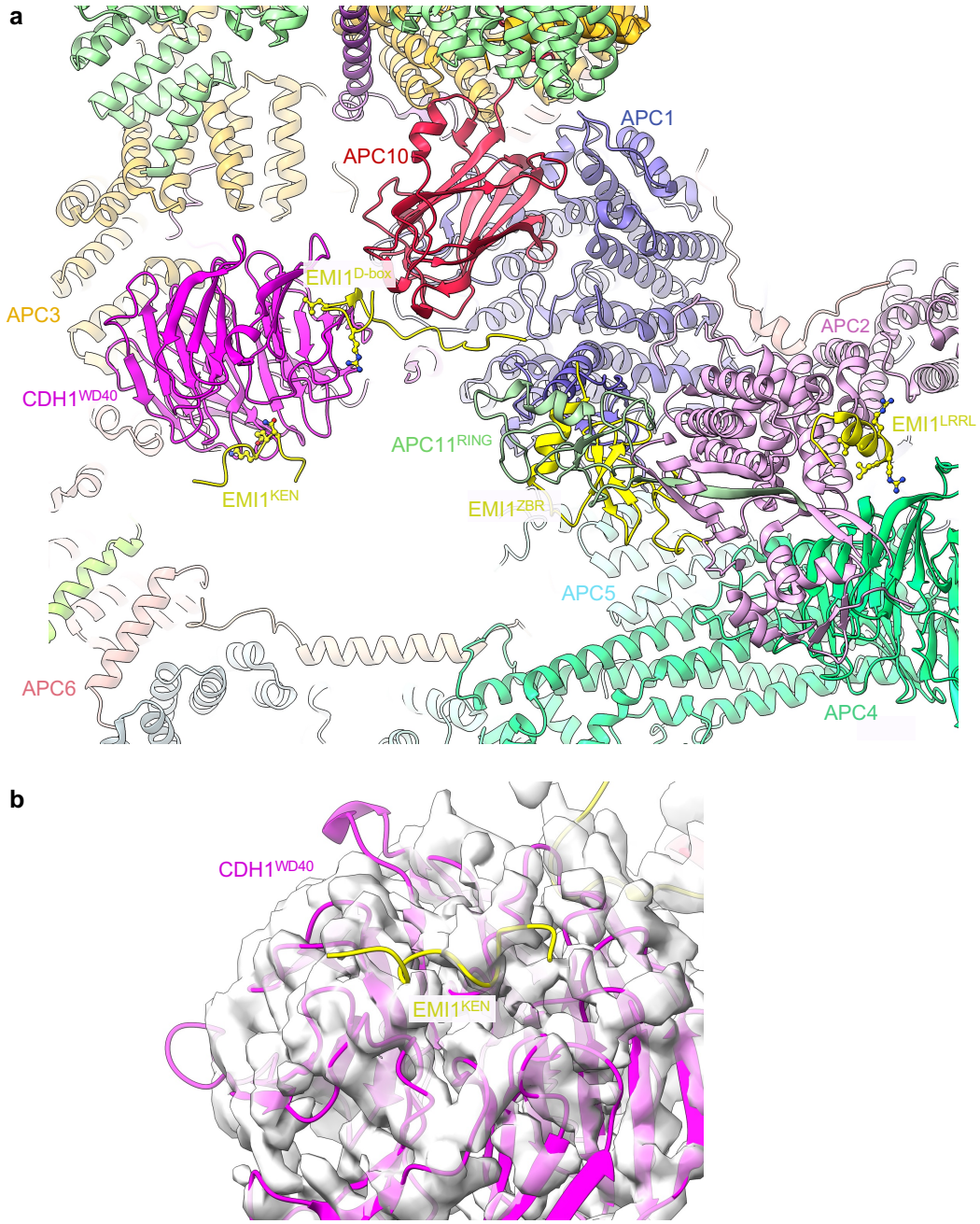

Figure 6. EMI1^{KEN} binding to CDH1. a, EMI1 binds to four sites on the APC/C$^{CDH1:EMI1}$ complex, thereby inhibiting APC/C^{CDH1} ubiquitination activity: (i) EMI1^{KEN} at the KEN box-binding site of CDH1^{WD40}, (ii) EMI1$^{D\text{-}box}$ at the D-box receptor, (iii) EMI1^{ZBR} to APC11^{RING}, and (iv) EMI1^{LRRL} to the APC2:APC4 interface. **b**, Cryo-EM density map of EMI1^{KEN} binding to CDH1^{WD40}.

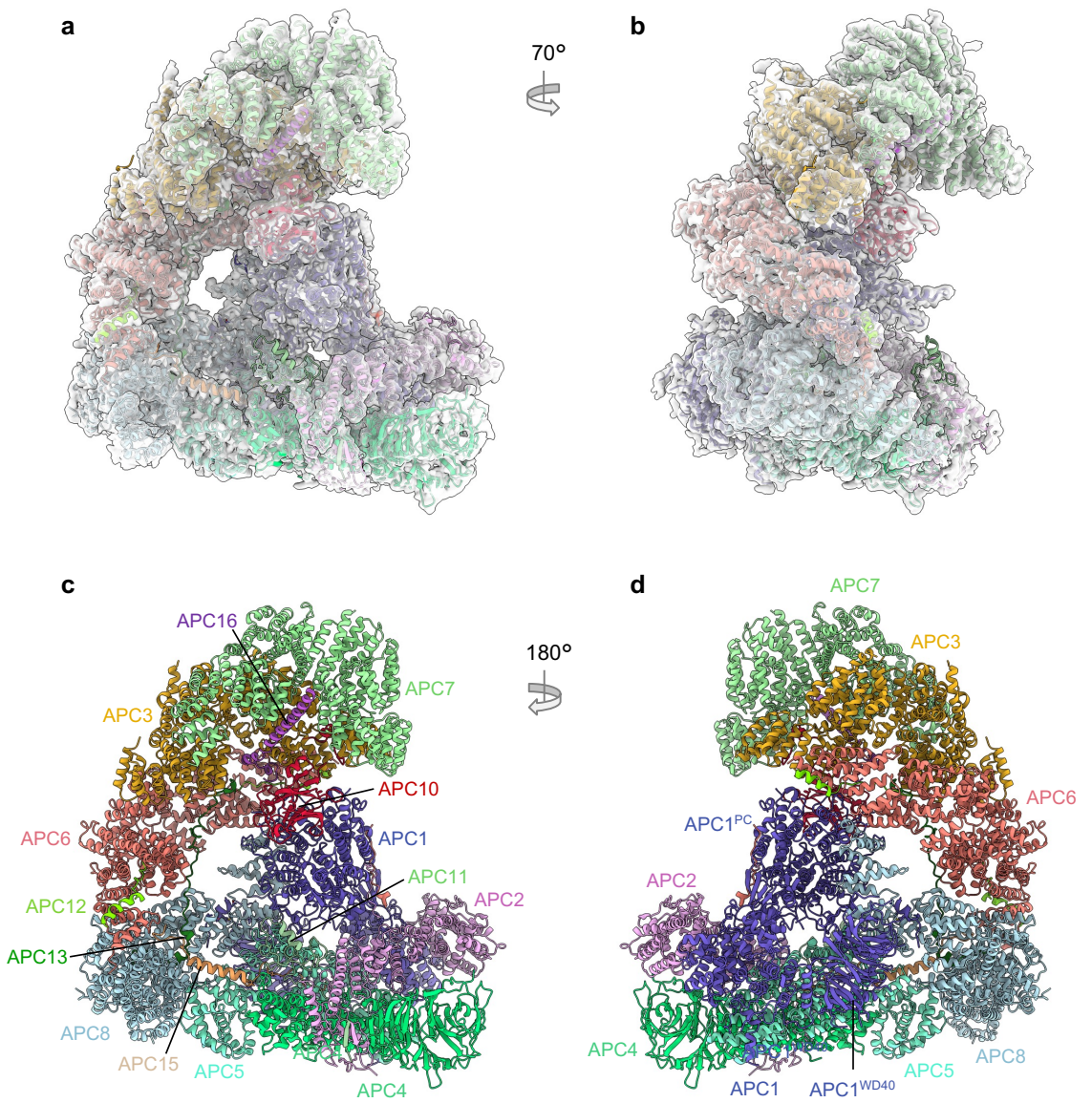

Figure 7. Overall structure of unphosphorylated apo-APC/C. a, and **b**, Two views of apo-APC/C fitted into the 3.2 Å cryo-EM map. **c**, and **d**, Two views of apo-APC/C shown as ribbons representations.

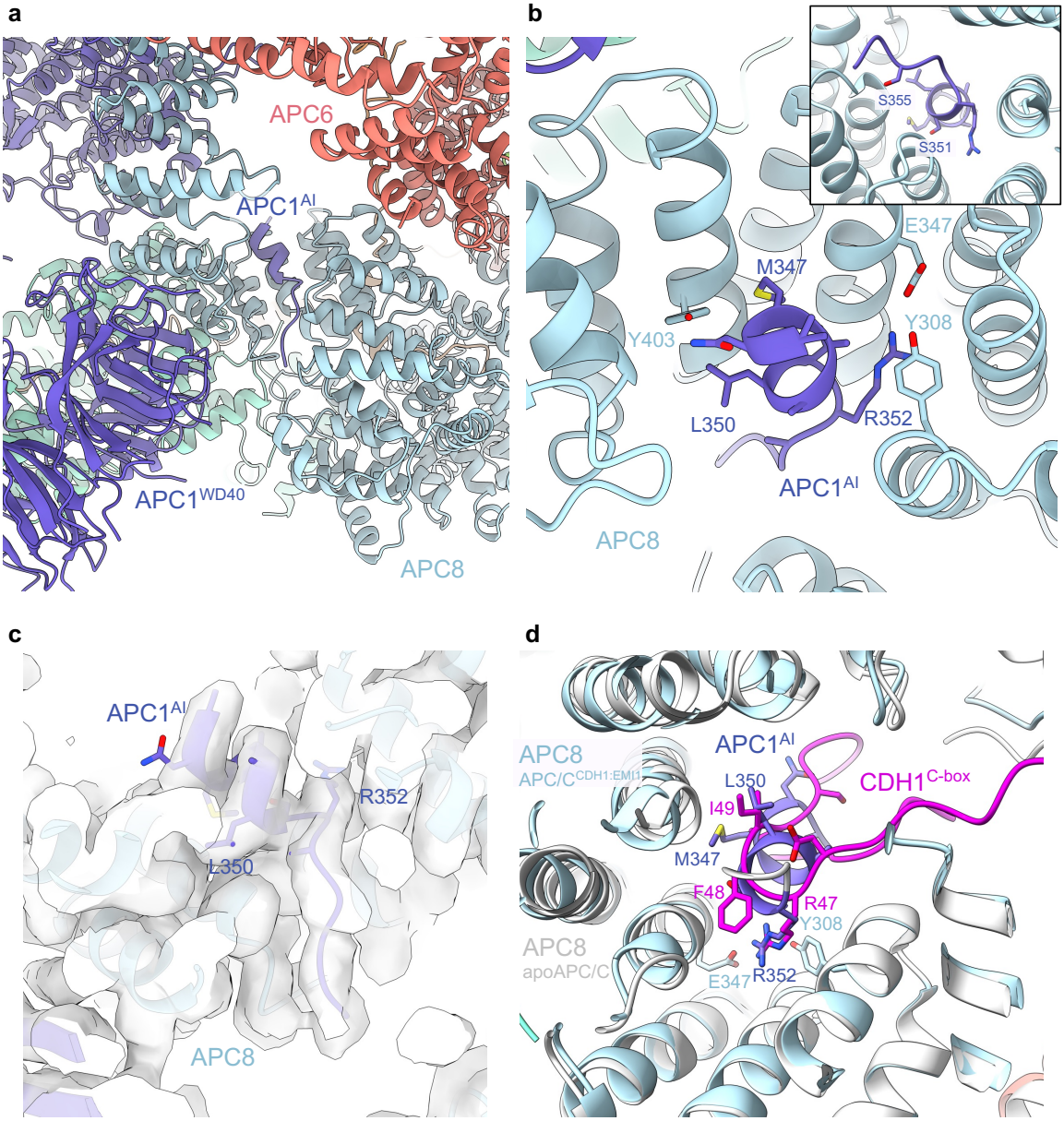

Figure 8. APC1^{AI} of unphosphorylated apo-APC/C. a, Overall figure showing APC1^{AI} at the C-box-binding site of APC8. **b**, Details of APC1^{AI} interactions at the C-box-binding site of APC8. **c**, Cryo-EM density map of APC1^{AI}. **d**, Superimposition of the unphosphorylated apo-APC/C (white) onto the APC/C$^{CDH1:EMI1}$ complex showing how the APC1^{AI} (slate blue) and CDH1$^{C\text{-}box}$ (magenta) overlap.